IMPLANTABLE ROBOTICS

Additive manufacturing of hydrogel-based materials for next-generation implantable medical devices

Sau Yin Chin,[1]*† Yukkee Cheung Poh,[1] Anne-Céline Kohler,[1] Jocelyn T. Compton,[2] Lauren L. Hsu,[1] Kathryn M. Lau,[1] Sohyun Kim,[1] Benjamin W. Lee,[1] Francis Y. Lee,[2‡] Samuel K. Sia[1]†

Implantable microdevices often have static components rather than moving parts and exhibit limited biocompatibility. This paper demonstrates a fast manufacturing method that can produce features in biocompatible materials down to tens of micrometers in scale, with intricate and composite patterns in each layer. By exploiting the unique mechanical properties of hydrogels, we developed a "locking mechanism" for precise actuation and movement of freely moving parts, which can provide functions such as valves, manifolds, rotors, pumps, and delivery of payloads. Hydrogel components could be tuned within a wide range of mechanical and diffusive properties and can be controlled after implantation without a sustained power supply. In a mouse model of osteosarcoma, triggering of release of doxorubicin from the device over 10 days showed high treatment efficacy and low toxicity, at $^1/_{10}$ of the standard systemic chemotherapy dose. Overall, this platform, called implantable microelectromechanical systems (iMEMS), enables development of biocompatible implantable microdevices with a wide range of intricate moving components that can be wirelessly controlled on demand, in a manner that solves issues of device powering and biocompatibility.

INTRODUCTION

Current additive manufacturing methods enable the rapid production of static three-dimensional (3D) structures (*1*). However, they exhibit some limitations that restrict their utility. First, they cannot easily generate structures with freely moving parts. Moving components, such as valves and pumps, require control in fabrication in the *z* axis, followed by the alignment and integration of unattached components. Second, current methods have limitations in constructing entirely biocompatible medical devices. Microelectromechanical systems (MEMS) devices (*2*–*5*) feature moving parts manufactured with methods developed for silicon and metals [such as thin-film deposition, photolithography, and etching (*6*)], but silicon-based materials present challenges as implantable devices because of their low biocompatibility (*7*–*9*). This limitation extends to implantable electronic devices that use silicon-based transistor circuits, which further require a reliable power supply via either a toxic battery or electronic interconnects between the interior and exterior of the body.

We sought to demonstrate that additive manufacturing can be developed to build biomaterial-based devices with freely moving parts that can be wirelessly controlled. Although there are various wireless modes of activation of implantable MEMS-based devices (such as electromagnetic methods, body-energy harvesting techniques, and ultrasonic powering), most reported methods involve the incorporation of electronic components that are nonbiocompatible (*10*–*12*). We chose poly(ethylene glycol) (PEG)–based hydrogels as building materials because they exhibit high biocompatibility and nonfouling properties, are flexible, and allow conformal contact to surrounding tissues; some have demonstrated safety in humans, with approval by the U.S. Food and Drug Administration (FDA) (*13*–*15*). These properties of hydrogels could impart new functionalities compared with other materials used in soft robotics, such as poly(dimethylsiloxane) (PDMS) (*16*–*18*). For example, in addition to their biocompatibility, some PEG-based hydrogels are biodegradable or can be synthetically modified to be biodegradable. PEG-based hydrogels can also be chemically modified or grafted with proteins, forming bioactive sites (*19*–*21*). Previously, photolithography and micromolding (*9*) have been used to form micropatterns of hydrogels, but the final structures tended to have a single layer of a single material (*22*–*24*) or to be devoid of moving parts (*25*–*28*). It has yet to be demonstrated that actively moving parts, inside multiple aligned and spatially complex 3D components, can be fabricated solely using hydrogels and can function in vivo. In addition to drug delivery, such techniques for processing biomaterials could, in the future, serve as an enabling platform for developing mechanically active hydrogel-based micromachines and soft robots that can interact with living systems (*29*, *30*).

RESULTS

Fabrication strategy

We developed a simple yet flexible and rapid setup for assembling layers of polymerized hydrogels (Fig. 1A and fig. S1). Layers could contain different biomaterial compositions and device components, including ones that can be controlled with an external magnet (Fig. 1B and fig. S2). Preformed hydrogel components that were separately fabricated using the same setup, including those that are doped with iron oxide nanoparticles, can also be easily aligned and incorporated to form a final integrated device. Magnetic actuation allows for wireless control and has been used clinically as a modality for controlling implantable medical devices (*31*). We devised this set of fabrication strategies to build implantable micromachines or iMEMS (implantable MEMS).

Specifically, our micromachining procedure consists of three steps: controlled movement in the *z* axis to determine the thickness of a layer, microfabrication of individual hydrogel layers, and selective release and bonding of adjacent layers. We used PEG diacrylate (PEGDA) to form PEG-based hydrogels, which are widely used, nontoxic, and nonfouling, some of which are FDA-approved (*32*) (specific compositions are shown in table S1). For controlled *z*-axis movement, we used a PDMS chamber with a thin flexible membrane coupled with a micrometer screw gauge via vacuum ports (Fig. 1A and fig. S1). This setup allowed us to create

---

[1]Department of Biomedical Engineering, Columbia University, 351 Engineering Terrace, 1210 Amsterdam Avenue, New York, NY 10027, USA. [2]Department of Orthopedic Surgery, Columbia University Medical Center, 622 West 168th Street, New York, NY 10032, USA.
*Present address: Molecular Engineering Laboratory, Biomedical Sciences Institute, 61 Biopolis Drive, #03-13 Proteos, Singapore 138673, Singapore.
†Corresponding author. Email: ss2735@columbia.edu (S.K.S.); sc2983@columbia.edu (S.Y.C.)
‡Present address: Department of Orthopedics and Rehabilitation, Yale University, 47 College Street Second Floor, New Haven, CT 06520, USA.

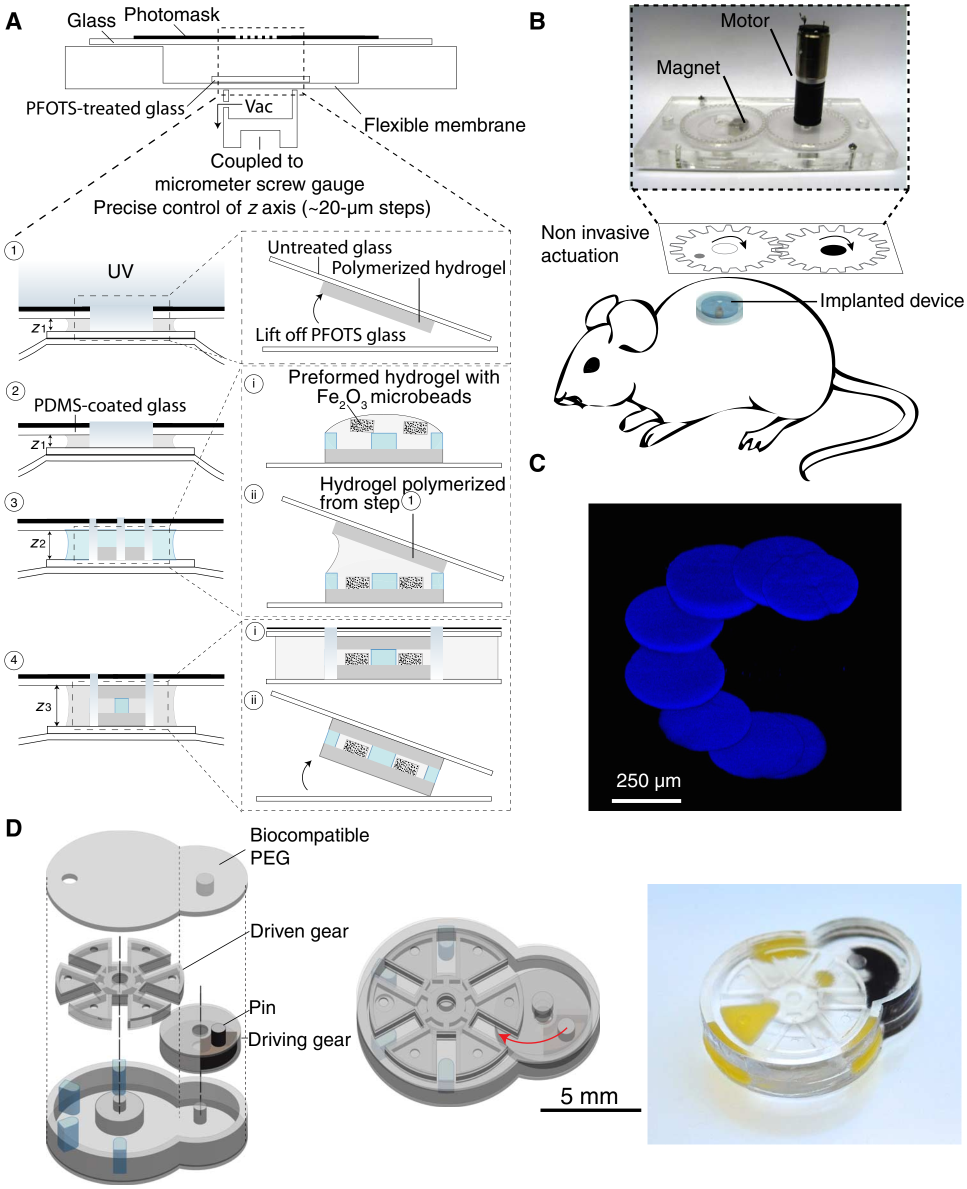

Fig. 1. Three-dimensional fabrication of implantable micromachines. (**A**) Photolithography and precise *z*-axis control via a stepper enables fabrication of multilayer hydrogel structures in the micrometer scale. (**B**) Upon subcutaneous implantation, the implantable MEMS device can be noninvasively and wirelessly actuated using an external motorized rotating magnet. (**C**) We fabricated a series of PEGDA discs in a spiral pattern to demonstrate the precision and the resolution of our technique with microfabricated structures. (**D**) Schematic diagram of an implantable hydrogel MEMS device made entirely of biocompatible PEGDA (a Geneva drive mechanism) (left) and an image of the fabricated device (right). The device contains iron nanoparticle–doped components, which respond to magnetic actuation. Actuation of device triggers release of payloads from reservoirs.

complex composite structures within one layer of the hydrogel and to control the thickness of each layer throughout the fabrication process. To fabricate multiple layers, we (i) polymerized and released a layer of hydrogel from trichloro(1*H*,1*H*,2*H*,2*H*-perfluorooctyl)silane (PFOTS)–treated glass (Fig. 1A, step 1); (ii) built layers of hydrogel as support structures (Fig. 1A, step 2); (iii) aligned prefabricated iron-oxide doped hydrogel structures (e.g., gears) onto the support structures (Fig. 1A, step 3i) and layered the polymerized hydrogel layer from step 1, ensuring proper alignment with the support structures (Fig. 1A, step 3ii); and (iv) photopolymerized it to seal the device and released it from untreated glass (Fig. 1A, step 4). We built a construct consisting of 15 aligned 50-µm-thick layers of PEGDA (8 of which contained fluorescently doped discs arranged to form a spiral pattern) (Fig. 1C). We also built structures from more complex designs, such as a Geneva drive (Fig. 1D), which is an intricate mechanism used in the mechanical watchmaking industry to implement precise intermittent movement. This complex structure was built within 30 min (table S2).

Design, fabrication, and actuation of versatile structures

We demonstrate that our fabrication strategy can be used to generate components and structures typically found in mechanical systems, such as a simple gate valve component (Fig. 2A), a gated linear manifold device (Fig. 2B), a spinning toothed rotor (Fig. 2C), and a spinning gear with multiple reservoirs (Fig. 2D). These structures represent typical components that are used in mechanical movement systems, including both linear (Fig. 2, A and B) and rotational (Fig. 2, C and D) movement. For linear movement, the placement of a magnet at one end generates movement of the iron-doped component; this mechanism is simple and works in vivo for a simple gate valve (Fig. 2A, right, and fig. S4). This mechanism can also be applied in a manifold, which contains multiple reservoirs for releasing payloads (Fig. 2B and movie S1). However, linear movement also requires dead spaces (i.e., spaces into which the iron-doped components move), which add to a larger footprint of the device.

Alternatively, our fabrication platform can also produce robust rotational movements, where the iron-doped component traverses through a cyclical path. In one design, a spinning toothed rotor (Fig. 2C, left) was fabricated in which the speed of rotation of the rotor can be reliably controlled [from 4 to 18 revolutions per minute (rpm)] by changing the voltage supplied to the motor of an external actuator (Fig. 2C, right). Mimicking a simple pump, we observed significantly higher velocities of beads in the solution around the gear when we increased the rotation frequency of the rotor (fig. S5). Moreover, this spinning toothed rotor can also be reliably actuated when implanted inside a euthanized mouse (fig. S6). In another design of rotational movement, payloads can move in concert with the iron-doped component (Fig. 2D). These designs feature minimal dead spaces and a decreased footprint of the device. We also developed two different methods for including superparamagnetic iron oxide nanoparticles into components (Fig. 2E). Bulk doping yields components that contain uniform but only moderate concentrations of nanoparticles; uniformly

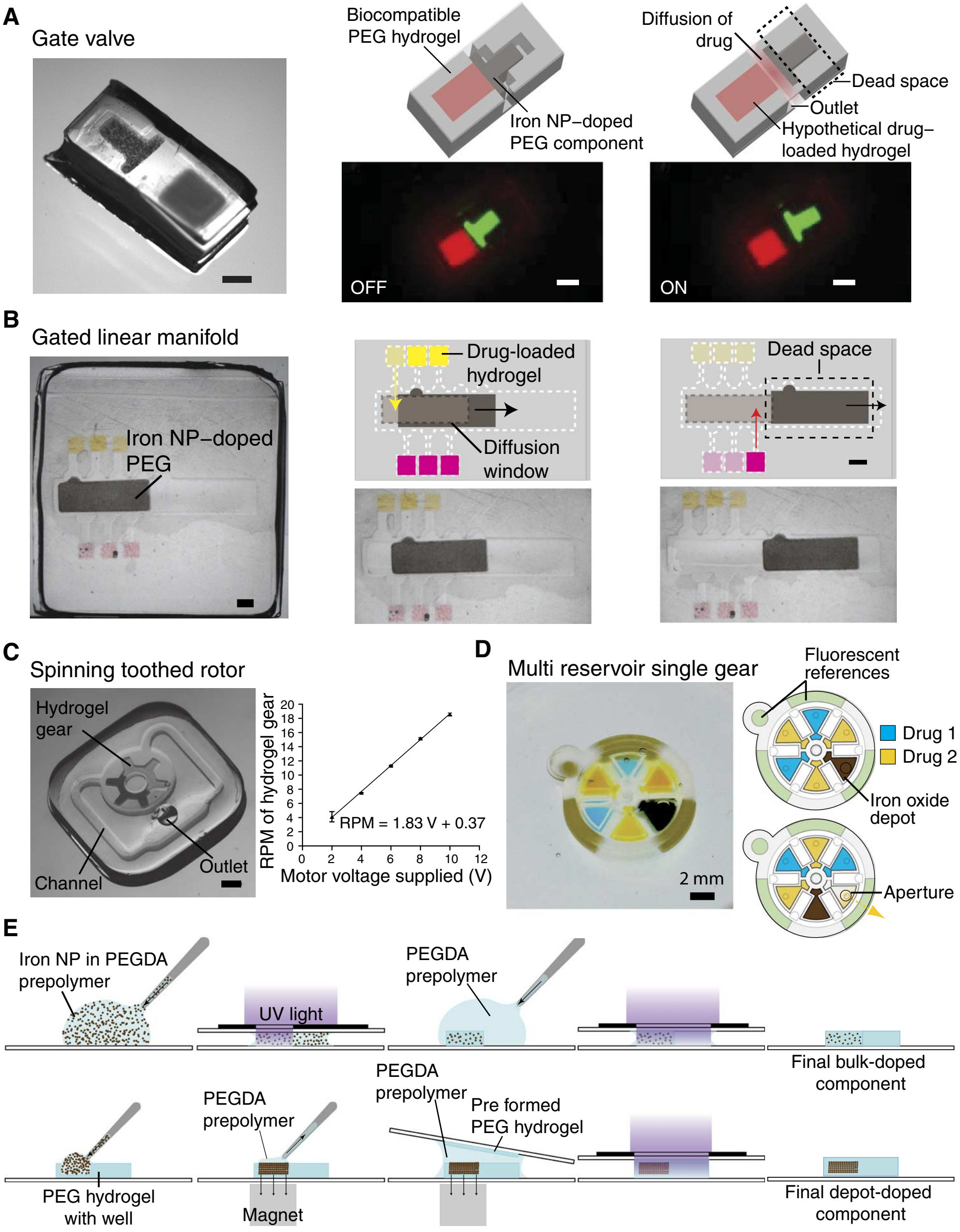

Fig. 2. Fabrication and actuation of versatile designs of components for hydrogel-based micromachines. (**A**) Picture of gate valve component (left), schematic diagrams (top), and corresponding in vivo imaging of the operation (right). This design consists of an iron nanoparticle (NP)–doped T-shaped plug and a reservoir with a hypothetical drug loaded in hydrogel; upon magnetic actuation, the T-shaped plug moves into the recess, allowing the drug to diffuse out of the construct via the outlet. For in vivo visualization, the T-shaped plug was doped with green fluorescent beads, and the drug-loaded hydrogel was doped with red fluorescent beads. The gate valve component was implanted subcutaneously in a euthanized nude mouse and imaged by a small-animal fluorescence imaging system within an hour after implantation. (**B**) Image of the gated linear manifold component (left), and schematic diagrams and corresponding pictures showing the operation. The manifold features six reservoirs; with each magnetic actuation, the plug moves in a stepwise fashion to the right and exposes a new pathway for diffusion of a hypothetical drug out of the device. (**C**) This design features rotational movement of a multilayer device constructed entirely out of PEG hydrogel, with a freely spinning toothed rotor in the center of a closed-loop microchannel. The hydrogel-based microgear was doped with iron oxide NPs. Graph (right) shows that the speed of rotation of the gear (rpm) can be controlled by changing the voltage supplied to the actuator (see figs. S2 and S6). Experimentally observed rotational speeds were based on $n = 4$ (multiple trials on the same device). Rotation of gear generated fluid flow within the surrounding microchannels (fig. S5), performing the function of a simple mixer and agitator for surrounding fluids. (**D**) Image (left) and schematic diagram (right) showing the operation of a multireservoir single gear. This rotational movement device contains a single gear, on which each of the six spokes contains a drug-loaded reservoir. Here, one reservoir is loaded with iron oxide NPs, and five reservoirs are loaded with different dye-infused gels. Each drug-containing reservoir has a small aperture that aligns to a larger aperture on the topmost layer of the device upon actuation. The iron-doped component and the reservoirs move in concert with each other during actuation and release, hence reducing the footprint of the device. (**E**) Two doping methods for incorporating iron oxide NPs into moving components. Bulk doping (top) works by polymerizing a suspension of iron oxide NPs in PEGDA prepolymer; this method features components with uniformly distributed iron oxide NPs. Depot doping (bottom) works by creating a well in PEG structures, followed by packing dense iron oxide NPs into the well as aided by a magnet, and sealing of the well by aligning and UV-polymerizing a preformed PEG hydrogel layer over the well.

mixing iron nanoparticles in prepolymer increases its opacity and hence decreases its ability to be photopolymerized, hence limiting the amount of nanoparticles that can be incorporated [~0.6% (v/v)]. On the other hand, depot doping (Fig. 2F) results in densely packed reservoirs of iron oxide nanoparticles [~25% (v/v)], which render components that are highly responsive to magnetism.

Leveraging hydrogel properties for versatile actuation

To support a versatile set of static and moving components to be used in complex devices, we investigated a range of PEG-based materials that can be used in this fabrication method (table S1). PEG-based materials have easily tunable mechanical and diffusive properties (Fig. 3A) (*14*, *33*–*35*). By varying the length of the PEG chain as well as the concentration (% w/v) of PEG used (Fig. 3B), the Young's moduli range from the order of 10 kPa (soft; similar to soft tissues) to 10 MPa (stiff; similar to rubber), with sustained mechanical strength with repeated testing over a 2-week period. In the Geneva drive design, we used a stiff PEG gel as a structural material for the exterior, support structures, and moving gears. We exploited the range of mechanical strength in another manner, by devising a robust "locking mechanism." This design features PEG components of complementary shapes but of differing mechanical strengths. As an initial example, a soft star-shaped axle holds a stiff gear

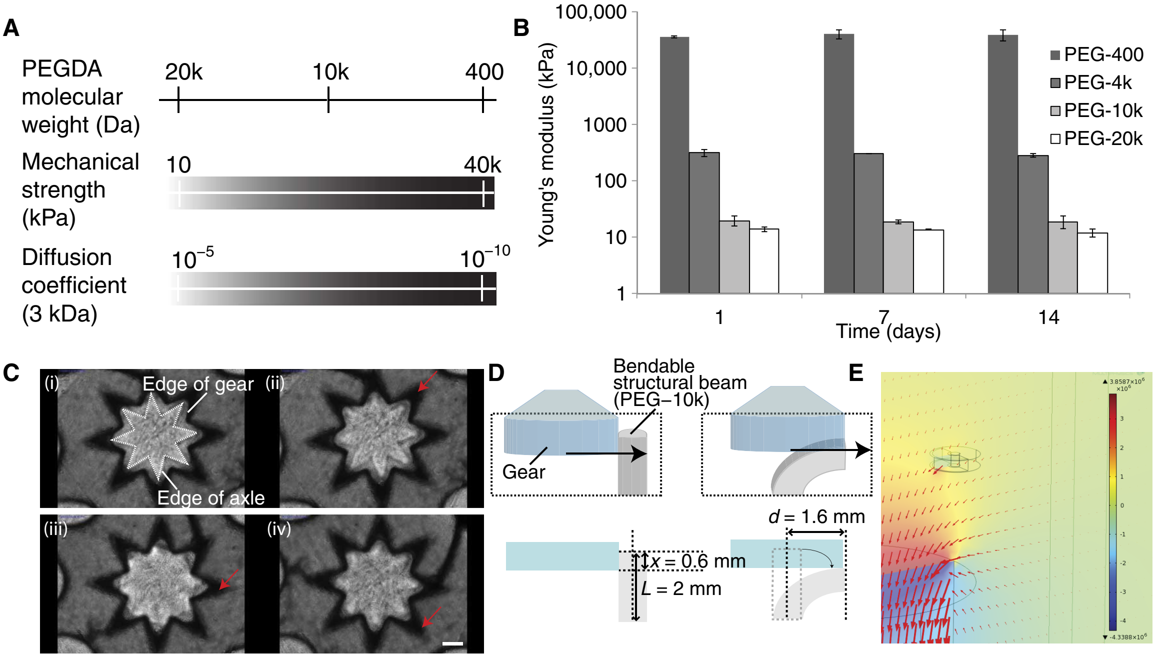

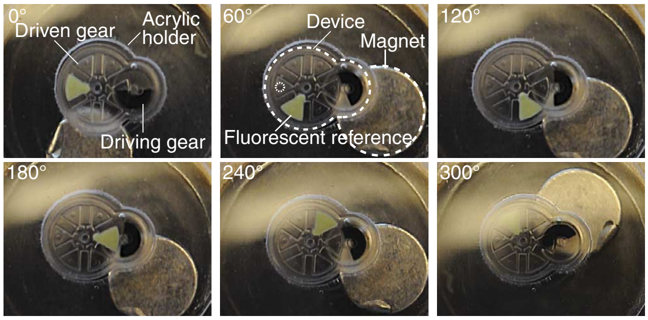

G

Type of hydrogel	Diffusion coefficient (D, cm²/s)		
	3-kDa dextran	20-kDa dextran	155-kDa dextran
PEG-400	Below LOD ($<10^{-10}$)	Below LOD ($<10^{-10}$)	Below LOD ($<10^{-10}$)
PEG-4k	4.7 ± 0.8 x 10^{-7}	1.0 ± 0.1 x 10^{-7}	Below LOD ($<10^{-10}$)
PEG-10k	1.2 ± 0.2 x 10^{-6}	5.9 ± 0.9 x 10^{-7}	8.7 ± 1.1 x 10^{-8}
PEG-20k	Above LOD ($>10^{-5}$)	5.3 ± 0.9 x 10^{-7}	2.5 ± 0.5 x 10^{-7}

Fig. 3. Material characterization and device performance in vitro. (**A**) Mechanical and diffusive properties of PEGDA hydrogels can be tuned by simply changing the molecular weight of PEGDA used. A large range of mechanical stiffnesses can be obtained by changing the PEGDA composition. (**B**) These hydrogels are also mechanically stable over 2 weeks because there is no appreciable decrease in the Young's modulus over time. (**C**) We used stiffness properties to achieve precise actuation. (i) A star-shaped axle (outlined) constructed from a softer gel is fitted with a gear constructed from a stiffer gel of a complementary shape. (ii) In the absence of magnetic actuation, the gear does not move and the star-shaped axle holds it in place. (iii) When the gear is magnetically actuated, it rotates and compresses the softer star-shaped axle. This deformation allows for further rotation of the device. (iv) When the gear has reached the desired position and magnetic actuation is removed, the star-shaped axle returns to its original shape and holds the gear in place. (**D**) The Geneva drive device is composed of two different types of hydrogels: a stiffer gel (PEG-400) that is used for the exterior of the device and gears and a softer gel (PEG-10k) that is used for posts that hold the driven gear in place during the absence of magnetic actuation. The schematic diagram shows an individual spoke/reservoir of the driven gear and its interaction with a neighboring soft post when viewed from the top (top) and cross section (bottom). The posts hold the gear in place but bend during actuation to allow for passage of the gear. The force required to bend the softer posts was calculated using simple beam-bending equations. (**E**) The geometries and material properties of neodymium magnets (N52), and driving gear with iron oxide depot were used to set up the COMSOL magnetic field simulation of the magnetic force acting on the driving gear. A calculated force of 0.7342 N was obtained via this simulation. (**F**) Time-lapse images show the operation of the device through all six "states" of the device. With each full rotation of the driving gear, the pin on the driving gear engages with one of the slots on the driven gear. In this manner, the driven gear, which contains reservoirs for payloads, is rotated by one position (60°), thereby aligning the next reservoir with an aperture that is located on the top of the device. (**G**) The permeability of the hydrogels can be tuned to achieve a wide range of diffusion coefficients (obtained via FRAP experiments). LOD, limit of detection.

in place, but actuation generates movement of the gear, which deforms the axle. Figure 3C and movie S2 show the operation of a star-shaped axle constructed out of softer PEG gels and a stiff PEG gear with a star-shaped bore.

Similarly, we used a locking mechanism for the Geneva drive device by incorporating soft PEGDA posts, which act as bendable posts (Fig. 3D); the posts fit between the spokes of the driven gear to keep it aligned in the absence of actuation but deform and bend to allow for rotation of the gear due to external force. From beam-bending equations, about 0.0039 N would be needed to bend all four posts (Fig. 3D), much less than the calculated magnetic force acting on the driving gear of 0.73 N (COMSOL simulations shown in Fig. 3E). In this manner, we were able to achieve precise actuation and movement of the Geneva drive (Fig. 3F), which consists of two engaged gears: a driving gear that is doped with iron oxide nanoparticles and a driven gear with six spokes. Each spoke of the Geneva drive contains a reservoir and an aperture that aligns with another aperture on the topmost layer of the assembled device with each 60° rotation. The smallest features in this design were 100 μm in the *xy* plane. These feature sizes enabled us to fabricate small reservoirs holding 200 to 600 nl of fluids. After the alignment of the gears, we sealed the entire construct with a final top layer to form the final assembled device (Fig. 1D, inset). The assembled Geneva gear device consisted of six layers (base layer, support for driven gear, axles for both gears, soft PEG posts, and two top layers), was about 5 mm tall and 15 mm in its longest dimension, and took a total of 30 min to manufacture (see table S2 for breakdown of time). By comparison, current commercial 3D methods (with print rates of millimeters to centimeters per hour) for printing a six-layer static polymeric structure would take several hours and would still be incompatible for use with soft hydrogel materials (*36*).

By rotating a magnet ~1 cm below the assembled device, one full rotation of the iron-doped driving gear results in a 60° rotation of the driven gear and a corresponding alignment of each reservoir with the aperture on the top layer (Fig. 3F and movie S3). When the driving gear was actuated with a permanent magnet, it engaged and moved a larger gear synchronously. This device was mechanically robust and could be actuated in vitro without mechanical failure for a period of at least 1 month, with dozens of rotations per day.

We also investigated the permeability of the materials as a design consideration for the device. For example, the hydrogel that lines a drug reservoir must be impermeable to the drug, whereas a different composition that is permeable to the drug may be used for other components. We performed fluorescence recovery after photobleaching (FRAP) experiments to determine the diffusion coefficients of the hydrogels; these experiments confirmed that the permeability of the hydrogel decreased with decreasing PEG chain length, as predicted (Fig. 3G, fig. S11, and table S3). For example, PEG-400 hydrogels would be appropriate as the walls of reservoirs that contain the drugs because they are impermeable to small molecules such as fluorescein isothiocyanate (FITC) (389 Da). Hence, a palette of mechanical strengths and diffusion coefficients could be obtained for the PEGDA components in the iMEMS device.

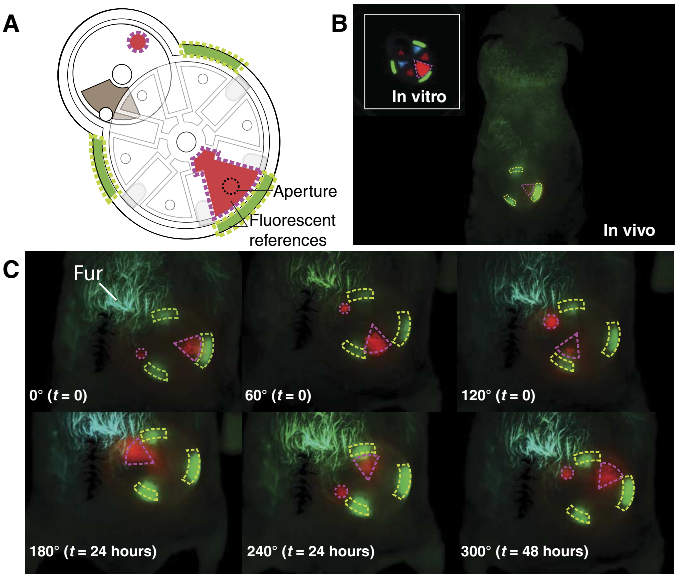

Fig. 4. In vivo movement of implantable MEMS device. (**A**) Schematic diagram of the Geneva drive device with payloads before implantation. Geneva drive devices are fabricated with fluorescent references (red and green fluorescent beads) to aid in vivo imaging to track the movement of the gears within the device. The reservoirs are filled with AF680-dextran and FITC-dextran solutions. (**B**) In vivo imaging shows the implanted Geneva drive device in the dorsum of the mouse. Fluorescent references are visible postimplantation. The device is in the "off" position. The inset shows the device as imaged by the Maestro Cri Imager before implantation. (**C**) Fluorescent images show operation of the Geneva drive device in an in vivo environment, including the position of the references within the device and hence the state of the device after each actuation. The animal protocol for this study was approved by the Institutional Animal Care and Use Committee of Columbia University.

In vivo actuation and localized low doses of chemotherapy in an osteosarcoma model

To investigate the functionality of the device in vivo, we implanted the Geneva drive device filled with two dyes (FITC-dextran and AF680-dextran) into the subcutaneous space of nude mice (Fig. 4A). We incorporated fluorescent references into the device so that the movement of the gears can be tracked via in vivo imaging (Fig. 4B). Over 2 days, for every full rotation of the driving gear, the driven gear reliably rotated 60° inside the mice (Fig. 4C), as intended by the intricate gear mechanism. This device also successfully delivered two different types of payloads (fig. S12).

Next, we tested the effectiveness of an iMEMS device in a mouse model of osteosarcoma. Clinically, patients who have undergone surgery to remove bone tumors are administered follow-up treatments with chemotherapy such as doxorubicin (*37*–*39*). This drug is toxic when administered systemically at high concentrations (*40*). We hypothesized that a localized delivery of chemotherapy at low doses, supplemented by the release of additional doses of drugs at any chosen time after implantation (e.g., in response to abnormal tumor growth and without further harming the patient), could be an efficacious form of treatment. Compared to constant release from simple polymer-based systems, such a pulsatile release of cancer drugs could better mimic the current regiments of chemotherapy, which is typically given in cycles (with periods of days to weeks) in order to best balance the targeting of rapidly proliferating cells in tumors while providing extra time for host cells to recover (*41*, *42*). An actively controlled system could also enable a clinician to adjust dosages dynamically to achieve this balance.

To this end, we used a single-gear design that was loaded with doxorubicin because its size is better suited for small-animal models. As a baseline, our device steadily releases doxorubicin at a low sublethal level (similar to most current drug-delivery devices), and magnetic actuation was performed to provide supplemental doses on demand after implantation. In an in vitro model, we found that the total doxorubicin released could be controlled by changing the actuation frequency (Fig. 5A). We demonstrated control from 20 to 90% release over 10 days (e.g., 45% by actuating the device every 4 days, and 87% by actuating it every 2 days); we anticipate that further changing the actuation frequencies would expand this range of control even further. Moreover, in passive-release systems, the release profiles are determined during the fabrication of the microspheres or scaffolds; once implanted, the release profiles cannot be changed or personalized. In the iMEMS device, the release profile can be controlled after the device is implanted by adjusting the actuation frequency.

Next, we tested the efficacy of this device in an in vivo osteosarcoma model, in which nude mice injected with human osteosarcoma cells (*43*, *44*) developed palpable tumors. We implanted the iMEMS device (carrying payloads of doxorubicin) subcutaneously and tracked in real time the growth of tumors by bioluminescence imaging (Fig. 5B) and the movement of gears by small-animal fluorescence imaging (fig. S23). We selected a local dose of doxorubicin at 10% of the standard systemic dose by estimating the mass of the tumor compared to body weight (*37*). We compared bioluminescence intensities (normalized to the intensity before treatment) for four different treatment groups: no treatment, high systemic dose (administered every 4 days), low systemic dose (administered every 2 days), and low local doses administered using

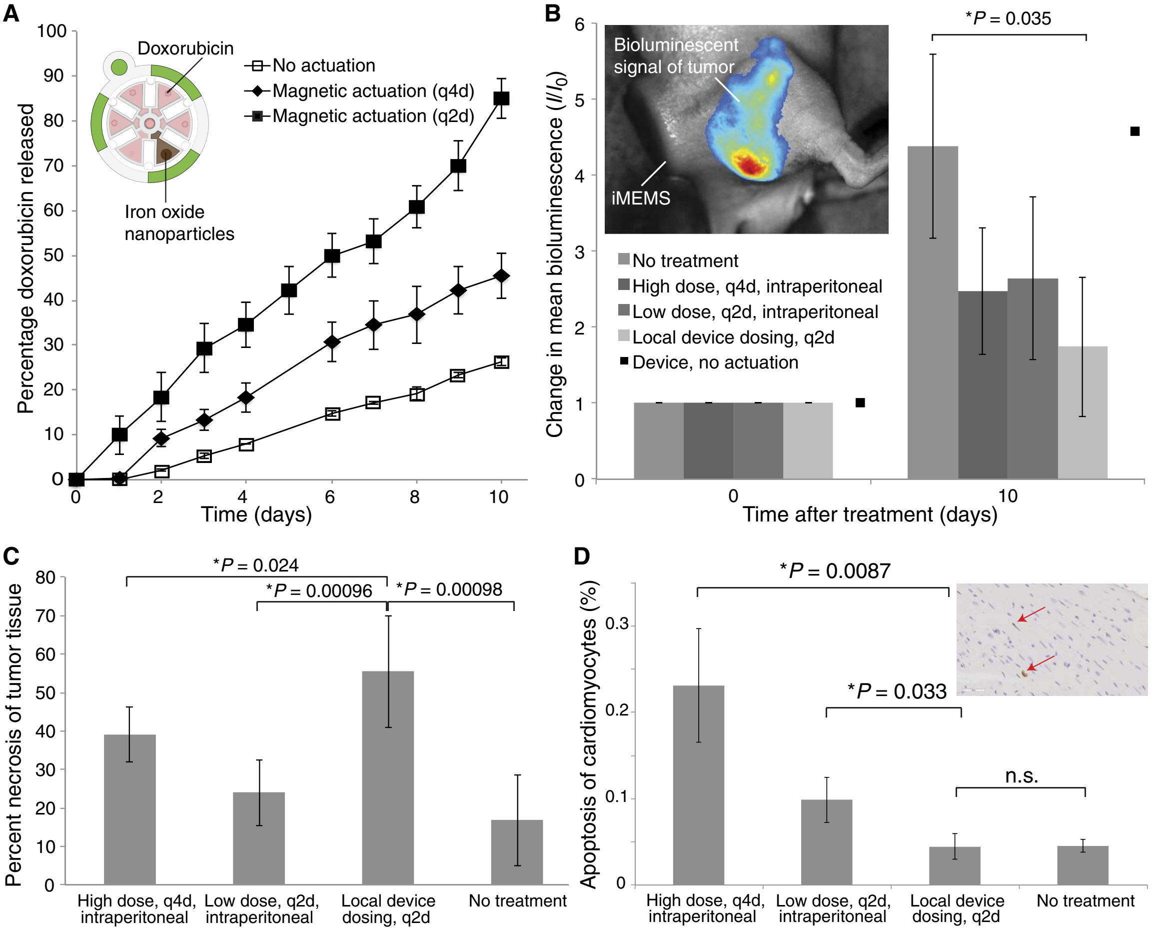

Fig. 5. iMEMS as a means for localized, low-dose chemotherapy for osteosarcoma. (**A**) In vitro release of doxorubicin from single-gear iMEMS device. Schematic diagram is shown in the inset. The device delivered five doses of doxorubicin, with each dose containing ~10% of a single conventional doxorubicin dose that would be administered systemically. We compared the release of doxorubicin from devices that were not actuated ($n = 3$), actuated once every 4 days (q4d, $n = 3$), and actuated once every other day (q2d, $n = 3$). Error bars show the SD for each averaged data point. (**B**) Change in tumor bioluminescent signal over time in a mouse osteosarcoma model treated with doxorubicin. Nude mice injected with luc-2–transfected osteosarcoma cells developed tumors that produced a bioluminescent signal in the presence of luciferin (inset). Doxorubicin-loaded devices were implanted close to the tumor site without interfering with the bioluminescent signal, and the growth of the tumor was tracked over time via bioluminescence imaging ($n = 3$). Tumor bioluminescent signals were tracked over 10 days for all treatment groups ($n = 3$ for each group). The graph shows the ratio of the average bioluminescent signal (photons per square centimeter per second) at days 0 and 10 to the signal at the start of treatment. Mice treated with the device showed the smallest increase in bioluminescent signal with a P value of 0.035. A one-tailed t test was used for statistical comparison. Error bars show the SD for each averaged data point. A single mouse ($n = 1$) was also implanted with a doxorubicin-loaded single-gear device but was not magnetically actuated (■). (**C**) The percentage necrotic area of the tumors for all treatment groups ($n = 3$ for each treatment group, three slices for each sample). Mice that were treated with local device dosing showed the highest percentage of tumor necrosis compared with all different treatment groups. (**D**) The percentage apoptosis of cardiomyocytes in mouse hearts (a measure of cardiotoxicity) after treatment with doxorubicin ($n = 3$ for each treatment group). The inset shows examples of apoptotic cardiomyocytes as detected via TUNEL staining. Ten sections per heart (at 40× magnification) were analyzed for apoptotic cells, and the percentage apoptotic to healthy cardiomyocytes was calculated. Mice that were treated with local device dosing showed lower levels of cardiotoxicity compared with other treatment groups ($^*P < 0.05$, one-tailed t test), and the percentage apoptosis of cardiomyocytes in this group was similar to that of mice that were not treated with doxorubicin. The animal protocol for this study was approved by the Institutional Animal Care and Use Committee of Columbia University. More information can be found in the Supplementary Materials. n.s., not significant.

the implanted iMEMS device (actuated every 2 days) (table S4). Compared with no treatment (*45*), treatment with high systemic doses resulted in a 44% inhibitory rate (comparable to literature values), whereas iMEMS local delivery resulted in a 60% inhibitory rate, the highest rate among all treatment groups (Fig. 5B). Moreover, we performed hematoxylin and eosin histological staining of the tumors at the distal end, middle, and proximal end of the femur to analyze tumor necrosis (*46*, *47*). Tumors from mice treated with high systemic doses showed necrosis of 39 ± 7%, those with low systemic doses showed necrosis of 19 ± 6%, and those treated with iMEMS showed necrosis of 56 ± 15% (Fig. 5C). A major side effect of doxorubicin is cardiotoxicity resulting from apoptosis of cardiomyocytes. We anticipated low side effects because iMEMS used only $^1/_{10}$ of the conventional high systemic dose. We analyzed the basal, midventricular, and apical sections of heart ventricles by TUNEL (terminal deoxynucleotidyl transferase–mediated deoxyuridine triphosphate nick end labeling) staining (*48*) for at least 10 fields of view for each sample (Fig. 5D). Mice treated with high and low systemic doses had 0.23 and 0.099% apoptotic cardiomyocytes, respectively, whereas those treated with iMEMS showed 0.045% apoptotic cardiomyocytes, which was comparable to mice that did not receive any doxorubicin (0.046%).

Overall, compared with a large dose of systemic chemotherapy, treatment of tumor-bearing mice with iMEMS-delivered local doses of doxorubicin resulted in the least tumor growth, greatest tumor necrosis, and lowest apoptosis of cardiomyocytes, and analysis of the excised device and surrounding tissue showed little to no inflammatory cells, no giant body cells (indicating the lack of chronic inflammation at the site of implantation), and the presence of a thin (<500 μm) fibrous capsule (indicating normal wound healing) (fig. S24).

DISCUSSION

The iMEMS method extends additive manufacturing to create a variety of moving parts (valves, manifolds, rotors, and pumps) in biocompatible microdevices, which forms the basis of many machines with advanced functions such as delivery of payloads. This method is based on simple and repeatable steps, enabled by a stepper mechanism, which allows for fabrication, alignment, and bonding of multiple intricately designed layers. Building on the potential of additive manufacturing for human health applications, the technology works with biomaterials that are well tolerated in the human body. Current methods for 3D printing of hydrogels (*49*) are limited to spatial resolutions above 200 μm at print speeds on the order of no more than millimeters per second for simple geometries (*50*) and cannot easily assemble structures with separate individual components, which may be needed for moving parts. The construction and demonstration of the in vivo function of the hydrogel-based Geneva drive, which features an intricate design wherein a driving gear must correctly engage a driven gear, strongly suggest that hydrogel materials, although often soft and compliant, can be tuned such that they make suitable materials for constructing complex MEMS-like devices. These data, especially the successful demonstration of force transmission within such devices, support the notion of hydrogels as a versatile basis material for soft robotics, alongside PDMS and other soft polymers (*16*, *51*, *52*). Previously, progress on producing polymeric microstructures that respond to stimuli has also been made (*53*, *54*), but the majority of it focused on individual components rather than on integrated devices. In future studies where biodegradation of the hydrogel devices is desired, biodegradable hydrogels (*55*, *56*) could be used, with the biodegradability of the device being triggered by enzyme or heat.

The iMEMS strategy addresses several fundamental considerations in building biocompatible microdevices, micromachines, and microrobots: how to power small robotic devices (because batteries are toxic), how to make small biocompatible moveable components (because silicon has limited biocompatibility), and how to communicate wirelessly once implanted (because radio frequency microelectronics require power, are relatively large, and are not biocompatible) (*2*, *57*). The entire iMEMS device consists of nontoxic components and does not require toxic batteries. Previous work on hydrogel drug release focused on the sustained release of one compound whose release profile must be determined before implantation (*58*–*60*) and often have more complicated (*61*, *62*) and invasive mechanisms for triggering delivery (*63*), with some concepts yet to show in vivo implementation (*61*, *63*). The iMEMS device can be triggered to release additional payloads over days to weeks after implantation (*60*). We achieved precise actuation by using magnetic forces to induce gear movements, which in turn bend structural beams made of hydrogels with highly tunable properties. Magnetic iron particles are commonly used and FDA-approved for human use as contrast agents (*64*, *65*). The ability to manufacture spatially complex biocompatible components, including freely moving parts, which can respond magnetically, enables continuous control and powering of the implanted microdevices without the need for onboard electronics or battery. In the future, such microscale components can be used for MEMS, larger devices (ranging from drug delivery to cardiac pacemakers) (*6*), and soft robotics (*29*, *30*).

Although passive release systems would still be useful for many disease scenarios, in cases of extensive solid tumors that fail to respond to low-dose chemotherapy and in the broader paradigm of personalized medicine where treatments are individualized according to the patient's dynamic health status, it would be critical to be able to tailor the therapy in an "on-demand" fashion, such that the therapy for each individual can be adjusted in real time depending on the growth of the tumor and the condition of the patient. This study takes a step toward that vision. To control cancer growth, a surgeon could insert this delivery device after surgical resection (i.e., near the margin where cancer frequently recurs), and thereafter in outpatient settings, the physician or even the patient could adjust the start of treatment and dosing schedule painlessly, after implantation of the device, depending on the growth of the tumor as revealed by real-time imaging. Should there be large tumors or multiple tumor sites, more than one device can be implanted at the time of biopsy. The surgeon could remove the devices or leave the device at the surgical field as long as it causes no inflammation. By effectively delivering low doses of drugs at the site of a tumor, the efficacy of standard chemotherapy can be increased while circumventing detrimental side effects such as cardiotoxicity. Our envisioned approach with an iMEMS device could either negate or supplement systemic chemotherapy, as shown in other cancers (*66*, *67*). In addition, our device would not require repeated injections of physical ablations (because it could be implanted under the currently scheduled biopsy under image guidance before chemotherapy and surgical resection), which may cause further spreading of cancer cells to surrounding healthy tissues. Compared with constant-release systems, the iMEMS approach could also prove particularly useful in clinical applications where pulsatile release is necessary (for example, in osteoporosis, constant delivery of the hormone would result in bone loss due to increased osteoclast activity (*57*).

To achieve clinical impact, multiple improvements can be made. First, designs that allow for payloads to be stored in solid or lyophilized phases could offer advantages in stability and decreased background release over time by decreasing convective leakage. Second, to further decrease the amount of background release from the device, designs with minimal spaces between moving layers could be implemented. Third, robustness of the actuation mechanism could be further increased: Although magnetic actuation of some implantable devices (such as vagus nerve stimulation) are in clinical use and normally robust (*31*) and our calculations confirm that the forces needed to move the gears are not felt under everyday conditions, future designs could increase the size or stiffness of support posts to enhance the locking mechanism. Moreover, a wearable device could sense the current spatial state of the device (via capacitive sensing of iron oxide nanoparticles or low-field electromagnetic sensing) and feed back to the actuator to ensure correct movement of device components.

Actuation of implanted components by magnetism could be particularly useful for interventions close to the skin surface, such as subcutaneous delivery (such as delivery of therapies for melanomas, wound healing, and scar prevention) or control over other superficially implanted systems (such as cerebral shunt systems). In the future, the iMEMS fabrication strategy could incorporate small implantable components responsive to other stimuli (such as temperature, pH, and light), including ultrasound, which could penetrate deep into the body (*68*).

In summary, we have demonstrated a strategy to manufacture biomaterials-based micromachines composed of moving components.

Through designs that feature a mixture of mechanical stiffnesses, we can wirelessly impart force transmission to components with mechanical stops, with end results of precise and robust movements. Additionally, these devices can be implanted safely into living hosts to effect environmental and physiological changes. These capabilities could find applications in drug delivery, applications that require control of microenvironments around delivered cells or engineered tissues, or implantable medical devices (such as stents) and could bring the field a step closer in developing soft miniaturized robots that can safely interact with humans and other living systems.

MATERIALS AND METHODS

Materials

PEGDA (molecular weight, 4000 and 400), FITC-labeled dextran (150 kDa), Fluoresbrite YG and YO Carboxylate Microspheres (diameter, 0.5 μm), and ProMag Superparamagnetic Microspheres (diameter, 3 μm) were purchased from Polysciences (Warrington, PA). PEGDA (molecular weight, 10,000 and 20,000) was purchased from Laysan Bio Inc. (Arab, AL). 2-Methyl-1-(4-(hydroxyethoxy)phenyl)-2-methyl-1-propanone (Irgacure 2959 or I2959) was obtained from Ciba (Tarrytown, NY). Darocur 1173 was obtained from Octochem Inc. (Vandalia, IL). 3-(Trimethoxysilyl)propyl methacrylate (TMSM), PFOTS, and 1-vinyl-2-pyrrolidone (NVP) were purchased from Sigma (St. Louis, MO). The OmniCure S2000 UV curing system and an adjustable collimating adaptor were purchased from EXFO (Canada). NdFeB disc magnets (diameter, 9.5 mm; height, 3 mm) were purchased from ForceField (Fort Collins, CO).

Preparation of hydrogel prepolymer

All hydrogel prepolymers used in this study consist of 10 to 90% (w/v) PEGDA (molecular weight, 400, 4000, 10,000, or 20,000), 1% (w/v) photoinitiator (I2959 or Darocur 1173), and 0.2% (v/v) NVP in phosphate-buffered saline. The specific compositions are listed in table S1. They were stored at 4°C and shielded from light until use.

Fabrication of hydrogel structure

To perform microfluidics-based lithography and to have precise control over the thickness of the microstructures, we used a PDMS fluidic device (19 mm × 19 mm × 1.3 mm) featuring a flexible bottom membrane (~250 μm thick), together with a custom-made *z*-axis stage that changes the height of the center chamber in precise micrometer movement (fig. S1, left). The fluidic device was secured onto the stage and the center chuck by vacuum. As the center chuck moved up and down, the bottom membrane flexed upward and downward accordingly, resulting in changes of height in the center chamber (fig. S1, right). Achievable heights ranged from 0 to 1.5 ± 2.5 μm. We bonded a piece of 1-cm × 1-cm cover glass (#2; ~190 to 230 μm thick) onto the bottom of the center chamber to ensure that the bottom remains flat at all times.

Surface treatment of glass substrate

All cover glasses were cleaned, bake-dried, and treated in oxygen plasma for 1 min before the application of silane. To promote hydrogel adhesion, cover glasses were immersed in 10% (w/v) TMSM (in 70% ethanol) for 1 hour. The cover glasses were rinsed three times in 100% ethanol and baked at 120°C for at least 10 min. To prevent hydrogel adhesion, cover glasses were treated with PFOTS vapor in a desiccator for 15 min. All treated cover glasses were stored in a desiccator before use. Alternatively, a thin layer of PDMS (<100 μm) was spun onto the cover glass to provide a nonadherent surface to the hydrogel.

Fabrication of hydrogel MEMS devices

The schematic of the fabrication steps is shown in Fig. 1A. Before fabrication, a clean PDMS fluidic device was placed on top of the fabrication platform (channel side faced up, as shown in fig. S1), where it was secured onto the stage via vacuum. A 50-mm × 35-mm #2 cover glass was placed on top of the PDMS fluidic device to form a closed channel. The micrometer was brought upward until the small cover glass (10 mm × 10 mm) attached to the bottom of the fluidic chamber (hereafter known as the bottom substrate) was in complete contact with the top cover glass. The respective *z* position was used as a reference zero point. This step was performed whenever a new PDMS fluidic device was used to account for any thickness variations. At this point, the bottom substrate was lowered, and the hydrogel prepolymer was drawn into the PDMS fluidic device using a syringe at the outlet. The bottom substrate was then raised until the fluidic chamber reached the desired height. A mask was placed directly on top of the top cover glass, and the hydrogel was exposed using a collimated ultraviolet (UV) light source (OmniCure S2000, EXFO) for 10 to 20 s. After this, the excess prepolymer was removed using a pipette or wicked away with filter paper, and a new hydrogel prepolymer was introduced for the subsequent cycle. The bottom substrate was adjusted to a new *z* position. A new mask was aligned with respect to the hydrogel microstructures formed in the previous cycle, and a new cycle of photopolymerization began. After the supporting structures were formed (which remained attached to the bottom substrate), the top cover glass was removed to allow the transfer of free-standing components (e.g., microgear) onto the supporting structures (Fig. 1A, step 3). Once the free-standing component was successfully transferred onto the supporting structures, the PDMS fluidic device was closed by a new cover glass to which a piece of preformed hydrogel was attached (Fig. 1A, step 4). As the bottom substrate was being adjusted to the new *z* position, an external magnet was used to guide the free-standing component to the desired position. Last, a new mask was used to photopolymerize selected regions on the hydrogel device, which joined the top hydrogel piece to the underlying supporting features. We removed uncross-linked precursors within voids to prevent swelling of hydrogel structures (especially for long-chain PEGs, which could swell about 10%) either by diffusion in the presence of a vacuum (for hydrogel devices with apertures that open to the surrounding medium) or by using fine-gauge needles to replace uncross-linked materials with buffer such that the puncture sites self-closed (in cases where the device was sealed from the surroundings). All fabricated devices were left to osmotically stabilize in saline or water before introduction of payload and use in vitro or in vivo.

All other methods (material characterizations, design and fabrication of specific designs, in vitro and in vivo actuation, and delivery of payloads) are included in the Supplementary Materials.

SUPPLEMENTARY MATERIALS

robotics.sciencemag.org/cgi/content/full/2/2/eaah6451/DC1
Methods
Fig. S1. Setup for microfluidics-based lithography with precise height control.
Fig. S2. Actuator for spinning hydrogel gears.
Fig. S3. COMSOL magnetic field simulation of the magnetic force acting on the driving gear.
Fig. S4. Gate valve design constructed out of PEG-based hydrogel.
Fig. S5. Microgear pump constructed using our fabrication strategy.
Fig. S6. A hydrogel microgear pump actuating inside a mouse.
Fig. S7. Fabrication of dextran-filled hydrogel "boxes" for in vitro diffusion assays.
Fig. S8. In vitro release of dextran encapsulated in PEGDA constructs.

Fig. S9. Graphs for early-time approximation of effective diffusion coefficient, D_{eff}.
Fig. S10. Graphs for late-time approximation of effective diffusion coefficient, D_{eff}.
Fig. S11. FRAP data.
Fig. S12. Dosing schedule for each mouse and the fluorescent signals detected at the end of each experiment.
Fig. S13. Linear movement design.
Fig. S14. Single rotating gears.
Fig. S15. Two-gear designs.
Fig. S16. Geneva drive design.
Fig. S17. Young's moduli for PEG-400 gels with increasing percentage of 400-Da PEGDA (w/v) used in the prepolymer.
Fig. S18. Young's moduli of polymerized PEGDA hydrogels with various PEG chain lengths.
Fig. S19. Schematic diagram of the Geneva drive device.
Fig. S20. In vitro release of different payloads from the Geneva drive device.
Fig. S21. Fabrication and complete assembly of a Geneva drive hydrogel MEMS device.
Fig. S22. Schematic diagram of the single-gear device.
Fig. S23. Subcutaneously implanted single-gear device in a tumor-bearing mouse.
Fig. S24. Explanted hydrogel MEMS device and histology of the surrounding tissue.
Fig. S25. Histology of bone tumor tissues.
Table S1. Gel compositions used in this study.
Table S2. Breakdown of the total time for constructing the Geneva drive device.
Table S3. Diffusion coefficients obtained from both FRAP experiments (D_{FRAP}) and in vitro release of dextran from fabricated hydrogel constructs (D_{eff}).
Table S4. Doxorubicin dosing schedule for different treatment groups.
Table S5. Device criteria and corresponding design considerations.
Movie S1. Actuation of a linear gated manifold device.
Movie S2. Operation of locking mechanism.
Movie S3. Rotation of the hydrogel-based Geneva drive gear.
References (*69–71*)

REFERENCES AND NOTES

1. J. R. Tumbleston, D. Shirvanyants, N. Ermoshkin, R. Janusziewicz, A. R. Johnson, D. Kelly, K. Chen, R. Pinschmidt, J. P. Rolland, A. Ermoshkin, E. T. Samulski, J. M. DeSimone, Additive manufacturing. Continuous liquid interface production of 3D objects. *Science* **347**, 1349–1352 (2015).
2. N. M. Elman, H. L. Ho Duc, M. J. Cima, An implantable MEMS drug delivery device for rapid delivery in ambulatory emergency care. *Biomed. Microdevices* **11**, 625–631 (2009).
3. H. Gensler, R. Sheybani, P.-Y. Li, R. Lo Mann, E. Meng, An implantable MEMS micropump system for drug delivery in small animals. *Biomed. Microdevices* **14**, 483–496 (2012).
4. X. Huang, C. Leduc, Y. Ravussin, S. Li, E. Davis, B. Song, D. Li, K. Xu, D. Accili, Q. Wang, R. Leibel, Q. Lin, A differential dielectric affinity glucose sensor. *Lab Chip* **14**, 294–301 (2014).
5. A. C. Tikka, M. Faulkner, S. F. Al-Sarawi, Secure wireless actuation of an implanted microvalve for drug delivery applications. *Smart Mater. Struct.* **20**, 105011 (2011).
6. A. C. R. Grayson, R. S. Shawgo, A. M. Johnson, N. T. Flynn, Y. Li, M. J. Cima, R. Langer, A BioMEMS review: MEMS technology for physiologically integrated devices. *Proc. IEEE* **92**, 6–21 (2004).
7. M. Frost, M. E. Meyerhoff, In vivo chemical sensors: Tackling biocompatibility. *Anal. Chem.* **78**, 7370–7377 (2006).
8. G. Voskerician, M. S. Shive, R. S. Shawgo, H. von Recum, J. M. Anderson, M. J. Cima, R. Langer, Biocompatibility and biofouling of MEMS drug delivery devices. *Biomaterials* **24**, 1959–1967 (2003).
9. K. M. Ainslie, T. A. Desai, Microfabricated implants for applications in therapeutic delivery, tissue engineering, and biosensing. *Lab Chip* **8**, 1864–1878 (2008).
10. S. Ozeri, D. Shmilovitz, Ultrasonic transcutaneous energy transfer for powering implanted devices. *Ultrasonics* **50**, 556–666 (2010).
11. M. A. Hannan, S. Mutashar, S. A. Samad, A. Hussain, Energy harvesting for the implantable biomedical devices: Issues and challenges. *Biomed. Eng. Online* **13**, 79 (2014).
12. A. Cadei, A. Dionisi, E. Sardini, M. Serpelloni, Kinetic and thermal energy harvesters for implantable medical devices and biomedical autonomous sensors. *Meas. Sci. Technol.* **25**, 012003 (2014).
13. N. A. Alcantar, E. S. Aydil, J. N. Israelachvili, Polyethylene glycol-coated biocompatible surfaces. *J. Biomed. Mater. Res.* **51**, 343–351 (2000).
14. G. M. Cruise, O. D. Hegre, F. V. Lamberti, S. R. Hager, R. Hill, D. S. Scharp, J. A. Hubbell, In vitro and in vivo performance of porcine islets encapsulated in interfacially photopolymerized poly(ethylene glycol) diacrylate membranes. *Cell Transplant.* **8**, 293–306 (1999).
15. T. R. Hoare, D. S. Kohane, Hydrogels in drug delivery: Progress and challenges. *Polymer* **49**, 1993–2007 2008).
16. J. C. Breger, C. K. Yoon, R. Xiao, H. Rin Kwag, M. O. Wang, J. P. Fisher, T. D. Nguyen, D. H. Gracias, Self-folding thermo-magnetically responsive soft microgrippers. *ACS Appl. Mater. Interfaces* **7**, 3398–3405 (2015).
17. F. Ilievski, A. D. Mazzeo, R. F. Shepherd, X. Chen, G. M. Whitesides, Soft robotics for chemists. *Angew. Chem. Int. Ed. Engl.* **50**, 1890–1895 (2011).
18. W. Jiang, D. Niu, H. Liu, C. Wang, T. Zhao, L. Yin, Y. Shi, B. Chen, Y. Ding, B. Lu, Photoresponsive soft-robotic platform: Biomimetic fabrication and remote actuation. *Adv. Funct. Mater.* **24**, 7598–7604 (2014).
19. M. L. Cuchiara, S. Coşkun, O. A. Banda, K. L. Horter, K. K. Hirschi, J. L. West, Bioactive poly(ethylene glycol) hydrogels to recapitulate the HSC niche and facilitate HSC expansion in culture. *Biotechnol. Bioeng.* **113**, 870–881 (2016).
20. J. A. Burdick, K. S. Anseth, Photoencapsulation of osteoblasts in injectable RGD-modified PEG hydrogels for bone tissue engineering. *Biomaterials* **23**, 4315–4323 (2002).
21. C. A. DeForest, K. S. Anseth, Advances in bioactive hydrogels to probe and direct cell fate. *Annu. Rev. Chem. Biomol. Eng.* **3**, 421–444 (2012).
22. J. W. Lee, J.-H. Park, M. R. Prausnitz, Dissolving microneedles for transdermal drug delivery. *Biomaterials* **29**, 2113–2124 (2008).
23. J.-H. Park, M. G. Allen, M. R. Prausnitz, Polymer microneedles for controlled-release drug delivery. *Pharm. Res.* **23**, 1008–1019 (2006).
24. W. Ryu, Z. Huang, F. B. Prinz, S. B. Goodman, R. Fasching, Biodegradable micro-osmotic pump for long-term and controlled release of basic fibroblast growth factor. *J. Control. Release* **124**, 98–105 (2007).
25. T. J. Hinton, Q. Jallerat, R. N. Palchesko, J. H. Park, M. S. Grodzicki, H. J. Shue, M. H. Ramadan, A. R. Hudson, A. W. Feinberg, Three-dimensional printing of complex biological structures by freeform reversible embedding of suspended hydrogels. *Sci. Adv.* **1**, e1500758 (2015).
26. S. P. Grogan, P. H. Chung, P. Soman, P. Chen, M. K. Lotz, S. Chen, D. D. D'Lima, Digital micromirror device projection printing system for meniscus tissue engineering. *Acta Biomater.* **9**, 7218–7226 (2013).
27. Y. F. Poon, Y. Cao, Y. Liu, V. Chan, M. B. Chan-Park, Hydrogels based on dual curable chitosan-*graft*-polyethylene glycol-*graft*-methacrylate: Application to layer-by-layer cell encapsulation. *ACS Appl. Mater. Interfaces* **2**, 2012–2025 (2010).
28. H. Tseng, M. L. Cuchiara, C. A. Durst, M. P. Cuchiara, C. J. Lin, J. L. West, K. J. Grande-Allen, Fabrication and mechanical evaluation of anatomically-inspired quasilaminate hydrogel structures with layer-specific formulations. *Ann. Biomed. Eng.* **41**, 398–407 (2013).
29. D. Rus, M. T. Tolley, Design, fabrication and control of soft robots. *Nature* **521**, 467–475 (2015).
30. S. Kim, C. Laschi, B. Trimmer, Soft robotics: A bioinspired evolution in robotics. *Trends Biotechnol.* **31**, 287–294 (2013).
31. P. Boon, K. Vonck, P. Van Walleghem, M. D'Havé, L. Goossens, T. Vandekerckhove, J. Caemaert, J. De Reuck, Programmed and magnet-induced vagus nerve stimulation for refractory epilepsy. *J. Clin. Neurophysiol.* **18**, 402–407 (2001).
32. R. Duncan, The dawning era of polymer therapeutics. *Nat. Rev. Drug Discov.* **2**, 347–360 (2003).
33. Y. K. Cheung, B. M. Gillette, M. Zhong, S. Ramcharan, S. K. Sia, Direct patterning of composite biocompatible microstructures using microfluidics. *Lab Chip* **7**, 574–579 (2007).
34. S. A. Lee, S. E. Chung, W. Park, S. H. Lee, S. Kwon, Three-dimensional fabrication of heterogeneous microstructures using soft membrane deformation and optofluidic maskless lithography. *Lab Chip* **9**, 1670–1675 (2009).
35. V. L. Tsang, S. N. Bhatia, Three-dimensional tissue fabrication. *Adv. Drug Deliv. Rev.* **56**, 1635–1647 (2004).
36. B. Mueller, Additive manufacturing technologies—Rapid prototyping to direct digital manufacturing. *Assembly Auto.* **32**, 10.1108/aa.2012.03332baa.010 (2012).
37. K. J. Widder, R. M. Morris, G. A. Poore, D. P. Howard, A. E. Senyei, Selective targeting of magnetic albumin microspheres containing low-dose doxorubicin: Total remission in Yoshida sarcoma-bearing rats. *Eur. J. Cancer Clin. Oncol.* **19**, 135–139 (1983).
38. B. Chiu, J. Coburn, M. Pilichowska, C. Holcroft, F. P. Seib, A. Charest, D. L. Kaplan, Surgery combined with controlled-release doxorubicin silk films as a treatment strategy in an orthotopic neuroblastoma mouse model. *Br. J. Cancer* **111**, 708–715 (2014).
39. H. Ma, C. He, Y. Cheng, Z. Yang, J. Zang, J. Liu, X. Chen, Localized co-delivery of doxorubicin, cisplatin, and methotrexate by thermosensitive hydrogels for enhanced osteosarcoma treatment. *ACS Appl. Mater. Interfaces* **7**, 27040–27048 (2015).
40. K. Chatterjee, J. Zhang, N. Honbo, J. S. Karliner, Doxorubicin cardiomyopathy. *Cardiology* **115**, 155–162 (2010).
41. E. Ricevuto, G. Bruera, P. Marchetti, General principles of chemotherapy. *Eur. Rev. Med. Pharmacol. Sci.* **14**, 269–271 (2010).
42. C. H. Takimoto, Basic pharmacokinetics and pharmacodynamic principles. *Cancer Treat. Res.* **106**, 85–101 (2001).
43. H. H. Luu, Q. Kang, J. K. Park, W. Si, Q. Luo, W. Jiang, H. Yin, A. G. Montag, M. A. Simon, T. D. Peabody, R. C. Haydon, C. W. Rinker-Schaeffer, T.-C. He, An orthotopic model of human osteosarcoma growth and spontaneous pulmonary metastasis. *Clin. Exp. Metastasis* **22**, 319–329 (2005).

44. K. Noh, K. Noh, K.-O. Kim, N. R. Patel, J. R. Staples, H. Minematsu, K. Nair, F. Y.-I. Lee, Targeting inflammatory kinase as an adjuvant treatment for osteosarcomas. *J. Bone Joint Surg. Am.* **93**, 723–732 (2011).
45. Y. Yang, X. Niu, Q. Zhang, L. Hao, Y. Ding, H. Xu, The efficacy of abraxane on osteosarcoma xenografts in nude mice and expression of secreted protein, acidic and rich in cysteine. *Am. J. Med. Sci.* **344**, 199–205 (2012).
46. G. Bacci, M. Mercuri, A. Longhi, S. Ferrari, F. Bertoni, M. Versari, P. Picci, Grade of chemotherapy-induced necrosis as a predictor of local and systemic control in 881 patients with non-metastatic osteosarcoma of the extremities treated with neoadjuvant chemotherapy in a single institution. *Eur. J. Cancer* **41**, 2079–2085 (2005).
47. P. Picci, T. Böhling, G. Bacci, S. Ferrari, L. Sangiorgi, M. Mercuri, P. Ruggieri, M. Manfrini, A. Ferraro, R. Casadei, M. S. Benassi, A. F. Mancini, P. Rosito, A. Cazzola, E. Barbieri, A. Tienghi, A. Brach del Prever, A. Comandone, P. Bacchini, F. Bertoni, Chemotherapy-induced tumor necrosis as a prognostic factor in localized Ewing's sarcoma of the extremities. *J. Clin. Oncol* **15**, 1553–1559 (1997).
48. K. Kyrylkova, S. Kyryachenko, M. Leid, C. Kioussi, Detection of apoptosis by TUNEL assay. *Methods Mol. Biol.* **887**, 41–47 (2012).
49. E. Malone, H. Lipson, Fab@Home: The personal desktop fabricator kit. *Rapid Prototyping J.* **13**, 245–255 (2007).
50. L. A. Hockaday, K. H. Kang, N. W. Colangelo, P. Y. Cheung, B. Duan, E. Malone, J. Wu, L. N. Girardi, L. J. Bonassar, H. Lipson, C. C. Chu, J. T. Butcher, Rapid 3D printing of anatomically accurate and mechanically heterogeneous aortic valve hydrogel scaffolds. *Biofabrication* **4**, 035005 (2012).
51. D. Morales, E. Palleau, M. D. Dickey, O. D. Velev, Electro-actuated hydrogel walkers with dual responsive legs. *Soft Matter* **10**, 1337–1348 (2014).
52. E. Palleau, D. Morales, M. D. Dickey, O. D. Velev, Reversible patterning and actuation of hydrogels by electrically assisted ionoprinting. *Nat. Commun.* **4**, 2257 (2013).
53. D. J. Beebe, J. S. Moore, J. M. Bauer, Q. Yu, R. H. Liu, C. Devadoss, B.-H. Jo, Functional hydrogel structures for autonomous flow control inside microfluidic channels. *Nature* **404**, 588–590 (2000).
54. J. Kim, S. E. Chung, S.-E. Choi, H. Lee, J. Kim, S. Kwon, Programming magnetic anisotropy in polymeric microactuators. *Nat. Mater.* **10**, 747–752 (2011).
55. J. A. Burdick, C. Chung, X. Jia, M. A. Randolph, R. Langer, Controlled degradation and mechanical behavior of photopolymerized hyaluronic acid networks. *Biomacromolecules* **6**, 386–391 (2005).
56. J. Kim, K.-W. Lee, T. E. Hefferan, B. L. Currier, M. J. Yaszemski, L. Lu, Synthesis and evaluation of novel biodegradable hydrogels based on poly(ethylene glycol) and sebacic acid as tissue engineering scaffolds. *Biomacromolecules* **9**, 149–157 (2008).
57. R. Farra, N. F. Sheppard Jr., L. McCabe, R. M. Neer, J. M. Anderson, J. T. Santini Jr., M. J. Cima, R. Langer, First-in-human testing of a wirelessly controlled drug delivery microchip. *Sci. Transl. Med.* **4**, 122ra21 (2012).
58. Z. Ulker, C. Erkey, An emerging platform for drug delivery: Aerogel based systems. *J. Control. Release* **177**, 51–63 (2014).
59. H. K. Makadia, S. J. Siegel, Poly lactic-*co*-glycolic acid (PLGA) as biodegradable controlled drug delivery carrier. *Polymers* **3**, 1377–1397 (2011).
60. X. Zhao, J. Kim, C. A. Cezar, N. Huebsch, K. Lee, K. Bouhadir, D. J. Mooney, Active scaffolds for on-demand drug and cell delivery. *Proc. Natl. Acad. Sci. U.S.A.* **108**, 67–72 (2011).
61. M. L. Noble, P. D. Mourad, B. D. Ratner, Digital drug delivery: On–off ultrasound controlled antibiotic release from coated matrices with negligible background leaching. *Biomater. Sci.* **2**, 893–902 (2014).
62. I. J. Bruvera, R. Hernández, C. Mijangos, G. F. Goya, An integrated device for magnetically-driven drug release and in situ quantitative measurements: Design, fabrication and testing. *J. Magn. Magn. Mater.* **377**, 446–451 (2015).
63. J. A. Floyd, A. Galperin, B. D. Ratner, Drug encapsulated aerosolized microspheres as a biodegradable, intelligent glioma therapy. *J. Biomed. Mater. Res. A* **104**, 544–552 (2016).
64. L. Johnson, S. E. Pinder, M. Douek, Deposition of superparamagnetic iron-oxide nanoparticles in axillary sentinel lymph nodes following subcutaneous injection. *Histopathology* **62**, 481–486 (2013).
65. Y.-X. J. Wang, Superparamagnetic iron oxide based MRI contrast agents: Current status of clinical application. *Quant. Imaging Med. Surg.* **1**, 35–40 (2011).
66. Z. Shen, T. Shen, M. G. Wientjes, M. A. O'Donnell, J. L. Au, Intravesical treatments of bladder cancer: Review. *Pharm. Res.* **25**, 1500–1510 (2008).
67. M. Westphal, D. C. Hilt, E. Bortey, P. Delavault, R. Olivares, P. C. Warnke, I. R. Whittle, J. Jaaskelainen, Z. Ram, A phase 3 trial of local chemotherapy with biodegradable carmustine (BCNU) wafers (Gliadel wafers) in patients with primary malignant glioma. *Neuro Oncol.* **5**, 79–88 (2003).
68. B. Trivedi, Microbiome: The surface brigade. *Nature* **492**, S60–S61 (2012).
69. S. Seiffert, W. Oppermann, Systematic evaluation of FRAP experiments performed in a confocal laser scanning microscope. *J. Microsc.* **220**, 20–30 (2005).
70. P. L. Ritger, N. A. Peppas, A simple equation for description of solute release I. Fickian and non-fickian release from non-swellable devices in the form of slabs, spheres, cylinders or discs. *J. Control. Release* **5**, 23–36 (1987).
71. L. Serra, J. Doménech, N. A. Peppas, Drug transport mechanisms and release kinetics from molecularly designed poly(acrylic acid-*g*-ethylene glycol) hydrogels. *Biomaterials* **27**, 5440–5451 (2006).

Acknowledgments: We thank K. Yeager for help with building the fabrication setup; C. Cheung for help with building the actuator; and O. Ordeig, T. Laksanasopin, B. Gillette, N. Tejavibulya, T. Guo, and S. Nayak for helpful scientific discussions. **Funding:** This work was supported by an NSF CAREER award, an NIH R01 grant (HL095477-05), and NSF ECCS-1509748. S.Y.C. was supported by the National Science Scholarship (PhD) awarded by the Agency for Science, Technology and Research (Singapore). **Author contributions:** S.Y.C., Y.C.P., A.-C.K., F.Y.L., and S.K.S. contributed to the conception and experimental design of the research. S.Y.C., Y.C.P., A.-C.K., L.L.H., K.M.L., J.T.C., and B.W.L. collected the data. S.Y.C., Y.C.P., A.-C.K., J.T.C., F.Y.L., and S.K.S. performed the data analysis and interpretation. J.T.C. and S.Y.C. prepared and implanted cell lines. A.-C.K., L.L.H., and S.K. refined manufacturing techniques for the devices. K.M.L. and A.-C.K. performed material characterizations. S.Y.C. and S.K.S. wrote the manuscript with support from all authors. **Competing interests:** The authors declare that they have no competing interests.

Submitted 26 July 2016
Accepted 30 November 2016
Published 4 January 2017
10.1126/scirobotics.aah6451

Citation: S. Y. Chin, Y. C. Poh, A.-C. Kohler, J. T. Compton, L. L. Hsu, K. M. Lau, S. Kim, B. W. Lee, F. Y. Lee, S. K. Sia, Additive manufacturing of hydrogel-based materials for next-generation implantable medical devices. *Sci. Robot.* **2**, eaah6451 (2017).

Science Robotics

Additive manufacturing of hydrogel-based materials for next-generation implantable medical devices

Sau Yin Chin, Yukkee Cheung Poh, Anne-Céline Kohler, Jocelyn T. Compton, Lauren L. Hsu, Kathryn M. Lau, Sohyun Kim, Benjamin W. Lee, Francis Y. Lee, and Samuel K. Sia

Sci. Robot. **2** (2), eaah6451. DOI: 10.1126/scirobotics.aah6451

Science Robotics (ISSN 2470-9476) is published by the American Association for the Advancement of Science. 1200 New York Avenue NW, Washington, DC 20005. The title *Science Robotics* is a registered trademark of AAAS.